



Article

# Synthesis of NiMoO<sub>4</sub>/3D-rGO Nanocomposite in Alkaline Environments for Supercapacitor Electrodes

Shahrzad Arshadi Rastabi <sup>1</sup>, Rasoul Sarraf Mamoozy <sup>1,\*</sup>, Fatemeh Dabir <sup>2</sup>,  
Nicklas Blomquist <sup>3</sup>, Manisha Phadataré <sup>3</sup> and Håkan Olin <sup>3</sup>

<sup>1</sup> Department of Materials Engineering, Tarbiat Modares University, 14115111 Tehran, Iran; Shd\_Arshadi@yahoo.com

<sup>2</sup> Non-Metallic Materials Research Group, Niroo Research Institute, 15119-43943 Tehran, Iran; fdabir@nri.ac.ir

<sup>3</sup> Department of Natural Sciences, Mid Sweden University, 85170 Sundsvall, Sweden; Nicklas.Blomquist@miun.se (N.B.); Manisha.Phadataré@miun.se (M.P.); Hakan.Olin@miun.se (H.O.)

\* Correspondence: rsarrafm@modares.ac.ir; Tel.: +98-912-133-4979

Received: 29 November 2018; Accepted: 3 January 2019; Published: 9 January 2019



**Abstract:** Although Graphene oxide (GO)-based materials is known as a favorable candidate for supercapacitors, its conductivity needs to be increased. Therefore, this study aimed to investigate the performance of GO-based supercapacitor with new methods. In this work, an ammonia solution has been used to remove the oxygen functional groups of GO. In addition, a facile precipitation method was performed to synthesis a NiMoO<sub>4</sub>/3D-rGO electrode with purpose of using synergistic effects of rGO conductivity properties as well as NiMoO<sub>4</sub> pseudocapacitive behavior. The phase structure, chemical bands and morphology of the synthesized powders were investigated by X-ray diffraction (XRD), Raman spectroscopy, and field emission secondary electron microscopy (FE-SEM). The electrochemical results showed that the NiMoO<sub>4</sub>/3D-rGO(II) electrode, where ammonia has been used during the synthesis, has a capacitive performance of 932 Fg<sup>-1</sup>. This is higher capacitance than NiMoO<sub>4</sub>/3D-rGO(I) without using ammonia. Furthermore, the NiMoO<sub>4</sub>/3D-rGO(II) electrode exhibited a power density of up to 17.5 kW kg<sup>-1</sup> and an energy density of 32.36 Wh kg<sup>-1</sup>. These results showed that ammonia addition has increased the conductivity of rGO sheets, and thus it can be suggested as a new technique to improve the capacitance.

**Keywords:** renewable energy systems; pseudocapacitive behavior; electrochemical results; ammonia; oxygen groups

## 1. Introduction

Growing concerns about the serious environmental pollution and fossil-fuel energy crisis have attracted considerable attention to renewable and clean energy storage technologies [1]. Lithium-ion batteries, sodium-ion batteries, and supercapacitors (SCs) are currently potential energy storage devices [2]. Among them, SCs have competitive characteristics, such as high power density, long cycle life, fast charging/discharging rate [3], high safety, simple operating principles, and low maintenance costs [4,5]. Various kinds of materials have been selected to improve electrode properties. Although carbonaceous materials such as graphene and reduced GO can deliver high power density and possess high specific-area, good electrical conductivity, high chemical stability, and biocompatibility [6], faradaic electrode materials like metal oxides can provide higher capacitance and larger energy densities due to their redox reactions [7]. Recently, binary nickel-based oxides have attracted tremendous research interest because of their high theoretical capacitance and excellent electrochemical activity [8], arising from their improved electronic conductivity and surface redox reactions. Among various pseudo-active materials, NiMoO<sub>4</sub> is an especially attractive candidate

for pseudocapacitors, offering good stability in alkaline electrolytes, high specific capacitance and accessibility [9]. Therefore, the motivation to design and fabricate an NiMoO<sub>4</sub> and rGO electrode with a novel hybrid nanostructure, which might combine the merits of both high specific capacitance originating from NiMoO<sub>4</sub> and excellent rate capability provided by rGO, is well founded.

Intensive studies have been carried out on the synthesis of NiMoO<sub>4</sub> with different morphologies such as nanorods [10], nanowires [11–13], nano-spheres [14], and nanosheets [15–17] for various application. Most of these studies used the hydrothermal method [8,10–15,18–25] that requires autoclave equipped with high-pressure and high-temperature, which finally resulted to the particles with large sizes and some of the papers used sonochemical [26], microwave [27], Sol-Gel [28], electrodeposition [17], and co-precipitation method [29,30]. Obviously, NiMoO<sub>4</sub> synthesis is much less achieved by chemical precipitation than the hydrothermal method. We also synthesized NiMoO<sub>4</sub> and graphene simultaneously for supercapacitor application, while those papers on chemical coprecipitation were exclusively for the synthesis of just NiMoO<sub>4</sub> and its photocatalyst properties. In the current work, a simple and low-cost chemical precipitation method was used to synthesize NiMoO<sub>4</sub>/3D-rGO nanocomposites with no need of any specific facilities. In addition, this work studies the mechanism of formation of NiMoO<sub>4</sub> nanoparticles on the surface of the graphene oxide and its reduction, which was not discussed in previous papers. Furthermore, there are several ways to reduce GO to rGO, one of which is the chemical reduction method. In previous works, various reduction agents such as hydrazine monohydrate [31], sodium borohydrate [32], ascorbic acid [33], ammonia borane [34], and heavy metal ions [35] have been used, while in the present research an ammonia solution has been applied.

In this work, we aim to synthesis the NiMoO<sub>4</sub>/3D-rGO electrode through a facile precipitation method for supercapacitors with particular emphasis on reduction of GO to rGO. Therefore, synergistic effects of ammonia, metal ions and low temperature have been used to eliminate large amount of GO oxygenated groups.

## 2. Experimental

### 2.1. Materials

Graphene oxide (GO), nickel nitrate hexahydrate (Ni(NO<sub>3</sub>)<sub>2</sub>·6H<sub>2</sub>O), sodium molybdate dihydrate (Na<sub>2</sub>MoO<sub>4</sub>·2H<sub>2</sub>O), and potassium hydroxide (KOH) were of reagent quality and were obtained from VWR, Sweden. Ammonia (28 wt. %-NH<sub>3</sub>) was purchased from VWR, Sweden. Polyvinylidene fluoride (PVDF, -(C<sub>2</sub>H<sub>2</sub>F<sub>2</sub>)<sub>n</sub>-), its solvent dimethylformamide (DMF, C<sub>3</sub>H<sub>7</sub>NO), and starch ((C<sub>6</sub>H<sub>10</sub>O<sub>5</sub>)<sub>n</sub>) were obtained from Sigma, Iran.

### 2.2. Preparation of the NiMoO<sub>4</sub>/3D-rGO(I) and NiMoO<sub>4</sub>/3D-rGO(II) Nanocomposites

Figure 1 briefly illustrates the fabrication of the NiMoO<sub>4</sub>/3D-rGO(II) nanocomposite through a simple precipitation process. The NiMoO<sub>4</sub>/3D-rGO composite was synthesized via a precipitation method in a starch environment as follows: First, 1 g of starch was added to 20 mL of distilled water at 80 °C to form a gelation suspension. Then, 1 mg of GO was dispersed in 20 mL distilled water under 5 min ultrasonication before being added to the starch solution to form a brown suspension. To prepare an alkaline environment, 3 mL ammonia (28 wt. %) was quickly added to the above suspension to adjust the pH about 10. Then, 5 mM Ni(NO<sub>3</sub>)<sub>2</sub>·6H<sub>2</sub>O and 5 mM Na<sub>2</sub>MoO<sub>4</sub>·2H<sub>2</sub>O were added to the above mixture in a dropwise manner and heated at 80 °C for 1 h, followed by 10 min of stirring. Subsequently, the powder was washed with distilled water to remove the impurities, and then dried at 60 °C for 24 h in a vacuum oven. Eventually, the final powder was calcinated in a tube furnace under Ar atmosphere at 350 °C for 2 h and then cooled to room temperature naturally to obtain the NiMoO<sub>4</sub>/3D-rGO(II) nanocomposite. The reduction of GO and the in situ formation of NiMoO<sub>4</sub> were achieved simultaneously, causing the generation of NiMoO<sub>4</sub>/rGO. The same process has been done without the addition of ammonia (NH<sub>3</sub>) and the sample is called NiMoO<sub>4</sub>/3D-rGO(I).

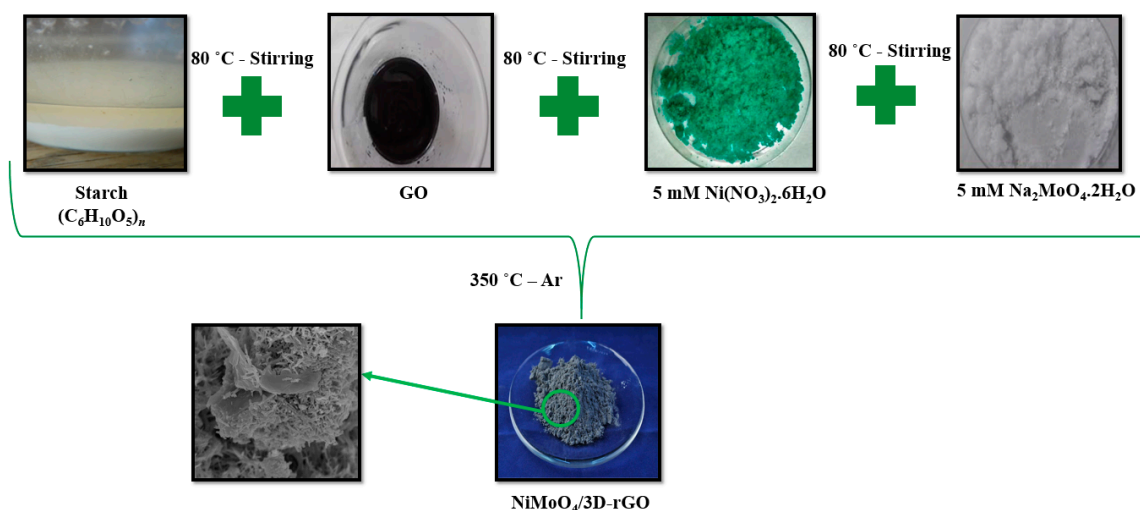


**Figure 1.** Schematic diagram of the synthesis process of  $NiMoO_4/3D-rGO(I)$ .

### 2.3. Electrode Fabrication of $NiMoO_4$ , $NiMoO_4/3D-rGO(I)$ , and $NiMoO_4/3D-rGO(II)$ Nanocomposites

The electrodes were prepared by mixing active material, carbon black, and polyvinylidene fluoride (PVDF) with a mass ratio of 80:10:10 in DMF, followed by ultrasonication of the slurry for 10 min to form a uniform solution. The Ni foam was cleaned with HCl (10 wt. %) and ethanol during ultrasonication. Then,  $2 \text{ mg} \cdot \text{cm}^{-2}$  of the mixture was pasted onto the Ni foam ( $1 \times 1 \text{ cm}^2$ ) as the working electrode before being dried in an oven at  $70 \text{ }^\circ\text{C}$  for 24 h.

### 2.4. Material Characterization

In this research, the following analytical systems were used to characterize the prepared powder. Structural characterization of the samples were characterized using an X-ray powder diffraction (XRD, Bruker with  $\text{CuK}\alpha$  radiation ( $\lambda = 0.1542 \text{ nm}$ ), Sundsvall, Sweden). Field-emission scanning electron microscopy (FE-SEM, MAIA3, TESCAN, Sundsvall, Sweden) was used to investigate the morphology and microstructure of the powder. Raman spectroscopy (Raman microscope, Horiba Xplora plus, laser excitation at  $532 \text{ nm}$ , Sundsvall, Sweden) in the frequency range of  $50\text{--}3000 \text{ cm}^{-1}$  was used to study the molecular bonds. A potentiostat system (VersaStat 4 with VersaStudio, Sundsvall, Sweden) was used to record the supercapacitor measurement.

## 3. Results and Discussion

X-ray diffraction analysis was used for studying the phase and structure of the samples. Figure 2 shows the XRD patterns of GO, rGO,  $NiMoO_4$  NPs,  $NiMoO_4/3D-rGO(I)$ , and  $NiMoO_4/3D-rGO(II)$  before and after calcination at  $350 \text{ }^\circ\text{C}$ . X-ray diffraction spectra of the samples were carried out at  $2\theta = 10^\circ\text{--}80^\circ$  with a scanning rate of  $0.02^\circ/\text{min}$ . As can be seen, GO has a sharp peak at  $2\theta = 10.6^\circ$  corresponded with the (002), which indicates the presence of the oxygen functional groups between the layers. This peak is disappeared in rGO pattern, implying the reduction of oxygen groups after heating at  $350 \text{ }^\circ\text{C}$ . The XRD pattern of the  $NiMoO_4$  NPs shows high intensity peaks, which implies the crystallinity of  $NiMoO_4$  nanoparticles. This pattern is in accordance with Card No 00-045-0142 of JCPDS (JCPDS or ICDD -International Centre for Diffraction Data) data and related to the monoclinic phase of  $NiMoO_4$ . The peaks at  $2\theta = 27.21^\circ$ ,  $30.36^\circ$ , and  $43.9^\circ$  which are the main characteristic peaks of the formation of the  $\alpha$ - $NiMoO_4$  phase, show that the sample after calcination is well crystallized and  $NiMoO_4 \cdot nH_2O$  has transformed to  $\alpha$ - $NiMoO_4$  [36]. Although the results indicate that most of the phases formed are related to the  $\alpha$ - $NiMoO_4$ , a number of peaks at  $2\theta = 21.12^\circ$ ,  $22.67^\circ$ , and  $32.07^\circ$  signifies the presence of the orthorhombic phase of  $Mo_{17}O_{47}$  (01-071-0566). These peaks are respectively attributed to the (510), (001), and (521) planes of  $Mo_{17}O_{47}$  phase. In fact,  $Mo_{17}O_{47}$  phase consists of seventeen  $MoO_3$  phases, which has lost some of its oxygen and formed a number of vacancies,

and eventually produced  $\text{Mo}_{17}\text{O}_{47}$  instead of  $\text{Mo}_{17}\text{O}_{51}$ . XRD pattern of the  $\text{NiMoO}_4/\text{3D-rGO(I)}$  shows the exact pattern of  $\alpha\text{-NiMoO}_4$ , with no diffraction peak of GO at  $2\theta = 10.6^\circ$ . The peak at  $2\theta = 22.67^\circ$  has been broadened rather than  $\alpha\text{-NiMoO}_4$  pattern, which is the same as rGO pattern. It can be concluded that in this case, the oxygenated groups of GO has been eliminated. The ammonia molecule is consisted of one nitrogen and three hydrogen atoms and due to the presence of lone pair on the nitrogen atom, this molecule is a strong source of electrons which is expected that it can eliminate oxygen groups of GO sheets. In order to investigate the role of the ammonia solution in the reduction process of GO, ammonia solution was added to GO suspension to adjust the pH about 10. After drying the sample at  $60^\circ\text{C}$  without further heat treatment, its color changed from brown to black. According to some papers, changing in color can be the evidence of converting GO into rGO [37]. This sample is characterized before and after calcination at  $350^\circ\text{C}$ . According to the XRD pattern of the  $\text{NiMoO}_4/\text{3D-rGO(II)}$  nanocomposite before calcination, there is no peak of GO at  $2\theta = 10.6^\circ$ , which indicates that before heat treatment, ammonia caused reduction of GO sheets. Furthermore, the XRD pattern of the  $\text{NiMoO}_4/\text{3D-rGO(II)}$  nanocomposite after calcination reveals a peak at  $43.3^\circ$ , which corresponds to N-rGO, based on data from [38]. It reveals that nitrogen of ammonia has been doped into the rGO network at  $350^\circ\text{C}$ . In addition, the peak at  $2\theta = 23.1^\circ$  ( $d \sim 3.4 \text{ \AA}$ ), while the GO has a peak at  $2\theta = 10.6^\circ$  ( $d \sim 8.3 \text{ \AA}$ ). The large space between the layers in GO is attributed to the presence of hydrocarbons, the oxygen-containing groups, and also the  $\text{H}_2\text{O}$  molecules at the edges and the distance between the sheets. In other words, decrease in the space between layers of graphene sheets in the  $\text{NiMoO}_4/\text{3D-rGO(II)}$  sample is a reason for the successful reduction of the GO sheets [39]. Results show that oxygen-containing groups can easily accept free electrons of ammonia to separate the carbon-oxygen bond, repaired  $\pi$  bands and form carbon radicals on GO sheets, and lead to the formation of rGO [37].

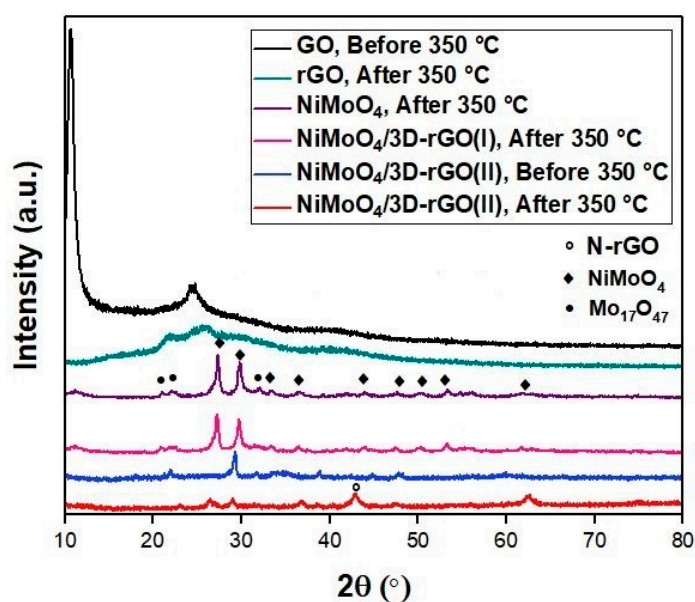
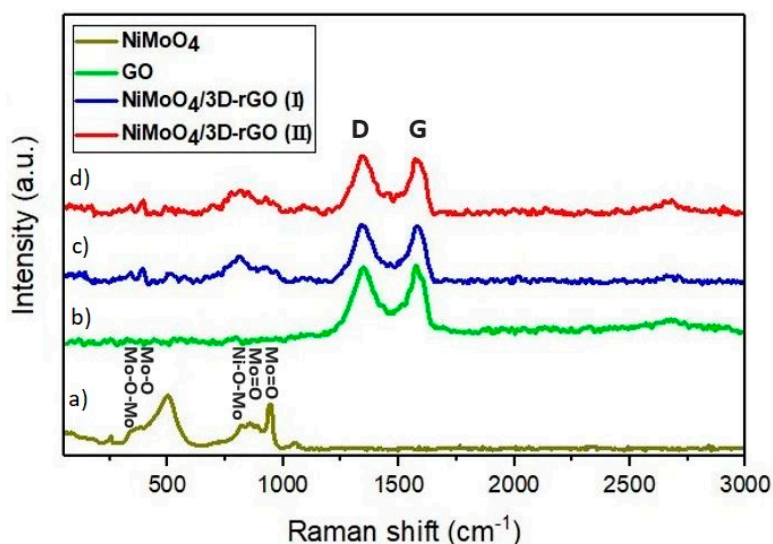


**Figure 2.** The XRD pattern of GO, rGO,  $\text{NiMoO}_4$  NPs,  $\text{NiMoO}_4/\text{3D-rGO(I)}$ , and  $\text{NiMoO}_4/\text{3D-rGO(II)}$  before and after heating at  $350^\circ\text{C}$ .

To compare the reduction rate of GO in the  $\text{NiMoO}_4/\text{3D-rGO(II)}$  nanocomposite with that of the  $\text{NiMoO}_4/\text{3D-rGO(I)}$  nanocomposite, the Raman spectra were measured for GO,  $\text{NiMoO}_4/\text{3D-rGO(I)}$ , and  $\text{NiMoO}_4/\text{3D-rGO(II)}$  nanocomposites (shown in Figure 2). The Raman spectra of the pure GO (Figure 3a) shows that the D and G peaks are located at  $1347.64 \text{ cm}^{-1}$  and  $1574.98 \text{ cm}^{-1}$ , respectively. The relative intensity ratio of the peaks ( $I_D/I_G$ ) is a measure of the disorder degree, and its value is approximately 0.98 for GO [23]. In both spectra of the  $\text{NiMoO}_4/\text{3D-rGO(I)}$  and  $\text{NiMoO}_4/\text{3D-rGO(II)}$  nanocomposites, the characteristic peaks at  $969 \text{ cm}^{-1}$  ( $\text{Mo=O}$ ),  $928 \text{ cm}^{-1}$  ( $\text{Mo=O}$ ),

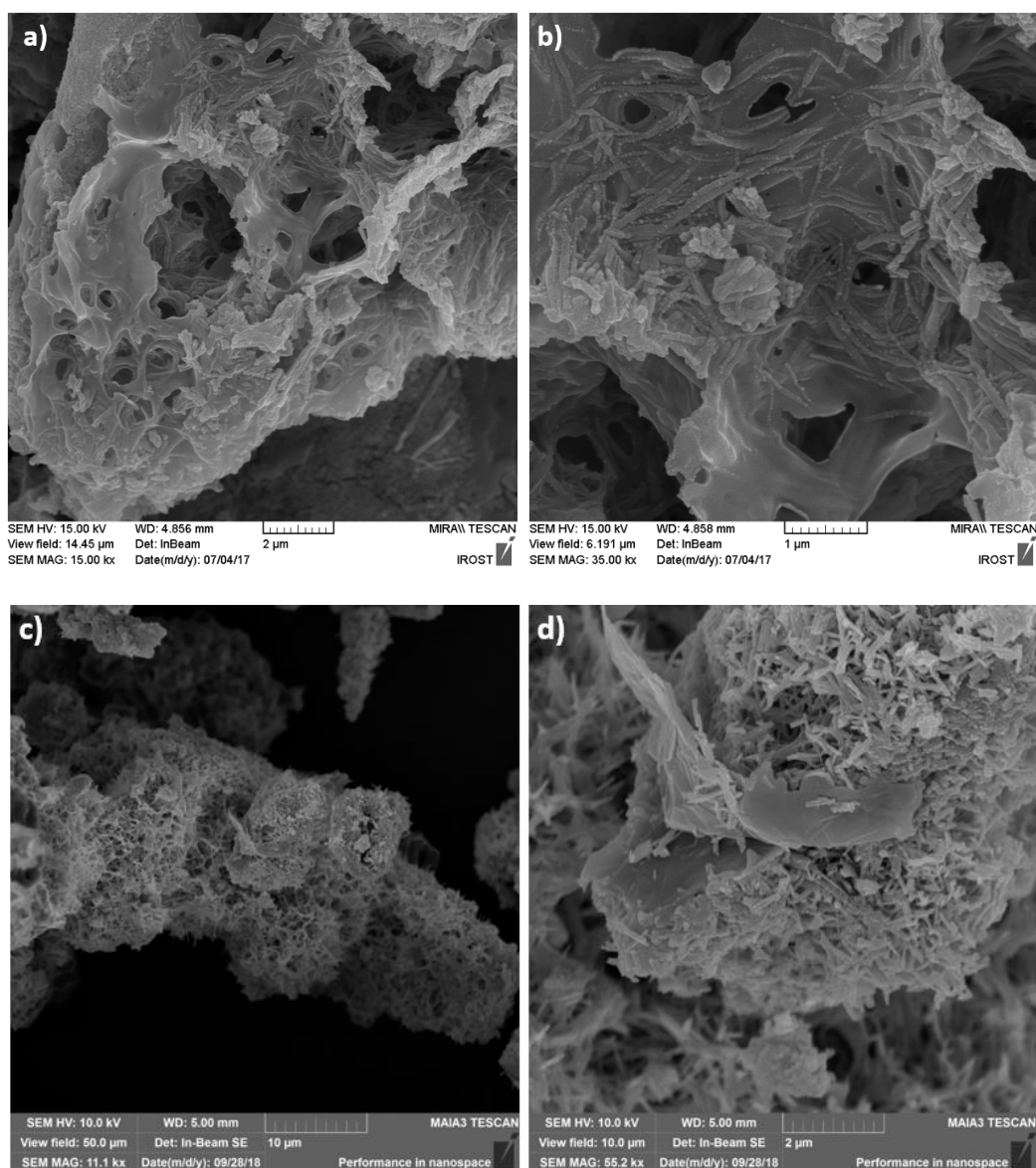


and  $697\text{ cm}^{-1}$  (Ni–O–Mo) and some medium-intensity peaks at  $394\text{ cm}^{-1}$  (Mo–O) and  $325\text{ cm}^{-1}$  (Mo–O–Mo) belong to the  $\alpha$ -phase  $\text{NiMoO}_4$  [10,40,41] according to  $\text{NiMoO}_4$  spectra (Figure 3a). The Raman spectra of the  $\text{NiMoO}_4/3\text{D-rGO(I)}$  nanocomposite (Figure 3b) shows that after chemical reduction of GO to rGO, the  $I_D/I_G$  ratio slightly increased from 0.98 (GO) to 1.02 (rGO), due to the increase in the amount of defects in rGO. In comparison to the  $\text{NiMoO}_4/3\text{D-rGO(I)}$ , the  $I_D/I_G$  ratio of  $\text{NiMoO}_4/3\text{D-rGO(II)}$  nanocomposite (Figure 3c) was calculated to be approximately 1.049, which is higher than that of the  $\text{NiMoO}_4/3\text{D-rGO(I)}$  nanocomposite (1.02). This finding shows that ammonia reduced more oxygenated groups in the  $\text{NiMoO}_4/3\text{D-rGO(II)}$  sample. In addition, the Raman spectra of the  $\text{NiMoO}_4/3\text{D-rGO(II)}$  nanocomposite (Figure 3c) shows that the D and G peaks redshifted to the wavenumbers at approximately  $1344.89\text{ cm}^{-1}$  and  $1574.98\text{ cm}^{-1}$ , respectively, compared to  $1339.39\text{ cm}^{-1}$  and  $1577.65\text{ cm}^{-1}$  in  $\text{NiMoO}_4/3\text{D-rGO(I)}$ . The Raman results confirm that although the GO has been reduced in the presence of  $\text{NiMoO}_4$  NPs, using an ammonia solution during synthesis results in more reduction of GO. In addition, the higher intensity of  $I_D/I_G$  in the  $\text{NiMoO}_4/3\text{D-rGO(II)}$  nanocomposite shows more defects and disorders in the rGO structure due to the removal of more functional groups on the surface of GO, which results in higher conductivity and provides more active sites for electron storage [23,42].



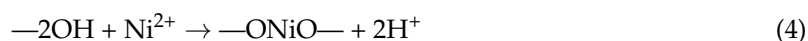
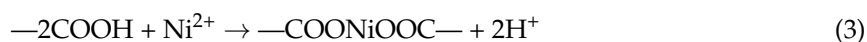
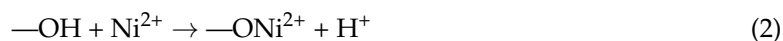
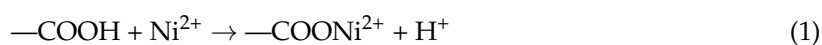
**Figure 3.** Raman spectra of the  $\text{NiMoO}_4$ , pure GO,  $\text{NiMoO}_4/3\text{D-rGO(I)}$ , and  $\text{NiMoO}_4/3\text{D-rGO(II)}$  nanocomposites.

The morphologies and microstructure of the prepared  $\text{NiMoO}_4/3\text{D-rGO(I)}$  and  $\text{NiMoO}_4/3\text{D-rGO(II)}$  nanocomposites were investigated by SEM (Figure 4). The SEM images of the both nanocomposites show a 3D interconnected network consisting of  $\text{NiMoO}_4$  nanorods and rGO sheets. According to the SEM images of  $\text{NiMoO}_4/3\text{D-rGO(I)}$  nanocomposite, it seems that graphene oxide sheets were the nucleation centers for growing  $\text{NiMoO}_4$  nanorods and they have been anchored the surface of reduced graphene sheets. This probably happened due to the strong electrostatic interaction between the nanorods and the reduced graphene oxide. Whereas the SEM images of  $\text{NiMoO}_4/3\text{D-rGO(II)}$  nanocomposite consisted of two different phases. It shows thick rGO sheets which can be interpret as graphite sheets. This phenomena can be attributed to the ammonia effect on reduction of the sheets. Another phase is  $\text{NiMoO}_4$  nanorods which due to magnetic interaction has gathered together and made a separate porous structure. The results showed that starch as an environmentally friendly surfactant prevented the agglomeration of particles and eventually turned into gases ( $\text{CO-CO}_2$ ) at  $350\text{ }^\circ\text{C}$  and resulted in a porous structure nanocomposite. Such a nanostructured morphology can provide more voids and a short diffusion path between the electrode material and the electrolyte which increases electrolyte diffusion and accessibility to reaction sites for more energy storage [23].



**Figure 4.** SEM images of (a,b) NiMoO<sub>4</sub>/3D-rGO(I) and (c,d) NiMoO<sub>4</sub>/rGO(II) nanocomposites with two different magnifications.

A possible formation mechanism for the synthesis of the NiMoO<sub>4</sub>/3D-rGO(I) nanocomposite is schematically shown in Figure 5. It is well known that,  $-\text{COOH}$  or  $-\text{OH}$  oxygen-containing functional groups of GO sheets are the nucleation centers for combining  $\text{Ni}^{2+}$  and  $\text{MoO}_4^{2-}$  ions to form NiMoO<sub>4</sub>. It has been reported that during the adsorption process, the release of the proton ( $\text{H}^+$ ) of  $-\text{COOH}$  or  $-\text{OH}$  functional groups to the solution results in a decrease of the equilibrium pH of the solution [43]. It can be concluded that the exchange of  $\text{Ni}^{2+}$  and  $\text{H}^+$  on  $-\text{COOH}$  or  $-\text{OH}$  oxygenated groups can be considered to be a mechanism for the adsorption of  $\text{Ni}^{2+}$  onto GO, and the formation of a bridge between different GO sheets. The relevant reactions in the current study can be expressed as follows:



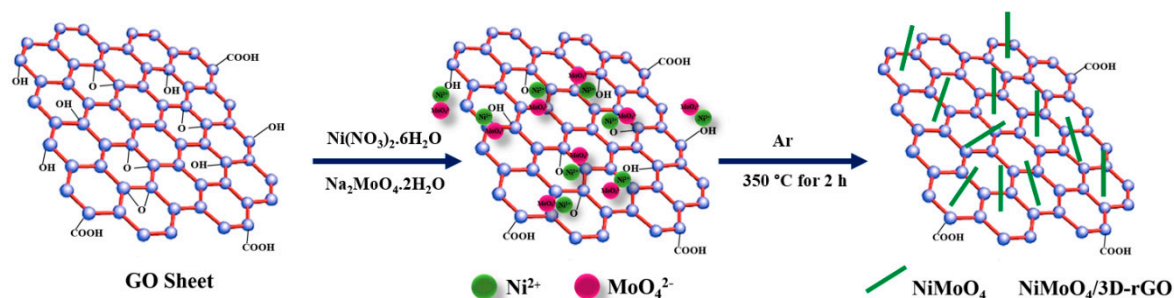
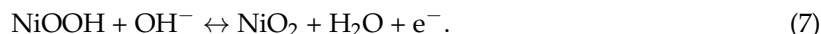
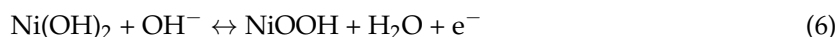


**Figure 5.** Schematic illustration of the fabrication process of hybrid NiMoO<sub>4</sub>/3D-rGO(I) nanocomposite.

### Electrochemical Studies

The electrochemical measurements of the samples were performed in a three-electrode cell configuration at room temperature with 3 M KOH electrolyte. In this system, a platinum sheet and a saturated calomel Hg/Hg<sub>2</sub>Cl<sub>2</sub> electrode were used as the counter and the reference electrodes, respectively. Cyclic voltammetry (CV) analysis was evaluated within a potential range of 0–0.7 V at different scan rates (10–100 mVs<sup>−1</sup>). Figure 6a shows the CV curves of the Ni foam, NiMoO<sub>4</sub> NPs, NiMoO<sub>4</sub>/3D-rGO(I), and NiMoO<sub>4</sub>/3D-rGO(II) nanocomposites. The redox peaks confirm that the charge-storage mechanism is mainly Faradaic (battery-type) and related to reversible chemical reactions of Ni(II) ↔ Ni(III) + e<sup>−</sup> [44] which can be expressed as follows [3,45]:



Mo atoms do not take part in the redox reaction. The main function of Mo element was to improve the conductivity of Nickel molybdate, thereby contributing in increasing specific capacitance and it does not show any redox peak in CV curves [46,47]. As seen, the area surrounded by the CV curve of the NiMoO<sub>4</sub>/3D-rGO(II) hybrid electrode is larger and the redox current is higher than that of the NiMoO<sub>4</sub>/3D-rGO(I) electrode, indicating much more specific capacitance of the NiMoO<sub>4</sub>/3D-rGO(II) electrode. More capacitance of NiMoO<sub>4</sub>/3D-rGO(II) supports the fact that removing more oxygenated surface functional groups of GO can provide more active sites for storing energy and increasing conductivity. Furthermore, the potential difference (ΔE) between the reduction and oxidation peaks of the NiMoO<sub>4</sub>/3D-rGO(II) composite is 160 mV, which is approximately 81 mV smaller than that of the NiMoO<sub>4</sub>/3D-rGO(I) electrode (241 mV, Figure 6a), indicating better electrochemical reversibility of NiMoO<sub>4</sub>/3D-rGO(II) due to more reduction of GO sheets in the presence of ammonia [48].

Figure 6b illustrates the CV curves of the NiMoO<sub>4</sub>/3D-rGO(II) electrode at the scan rates of 10–100 mVs<sup>−1</sup> in the potential window of 0–0.7 V. With increased scan rates, the anodic and cathodic currents increase, suggesting fast redox reactions at the electrode/electrolyte contact surface at high scan rates, which results in lower specific capacitance [22]. Due to the presence of graphene oxide sheets, in addition to the Faradaic and electrochemical reactions of NiMoO<sub>4</sub>, formation of the electrical double-layer can lead to more charge storage in the system [49]. According to the resulting curves, it is noteworthy that by increasing the scan rate, even at the scan rate of 100 mVs<sup>−1</sup>, redox peaks are still observed, indicating good chemical stability and conductivity in the hybrid structure of the electroactive materials [50].

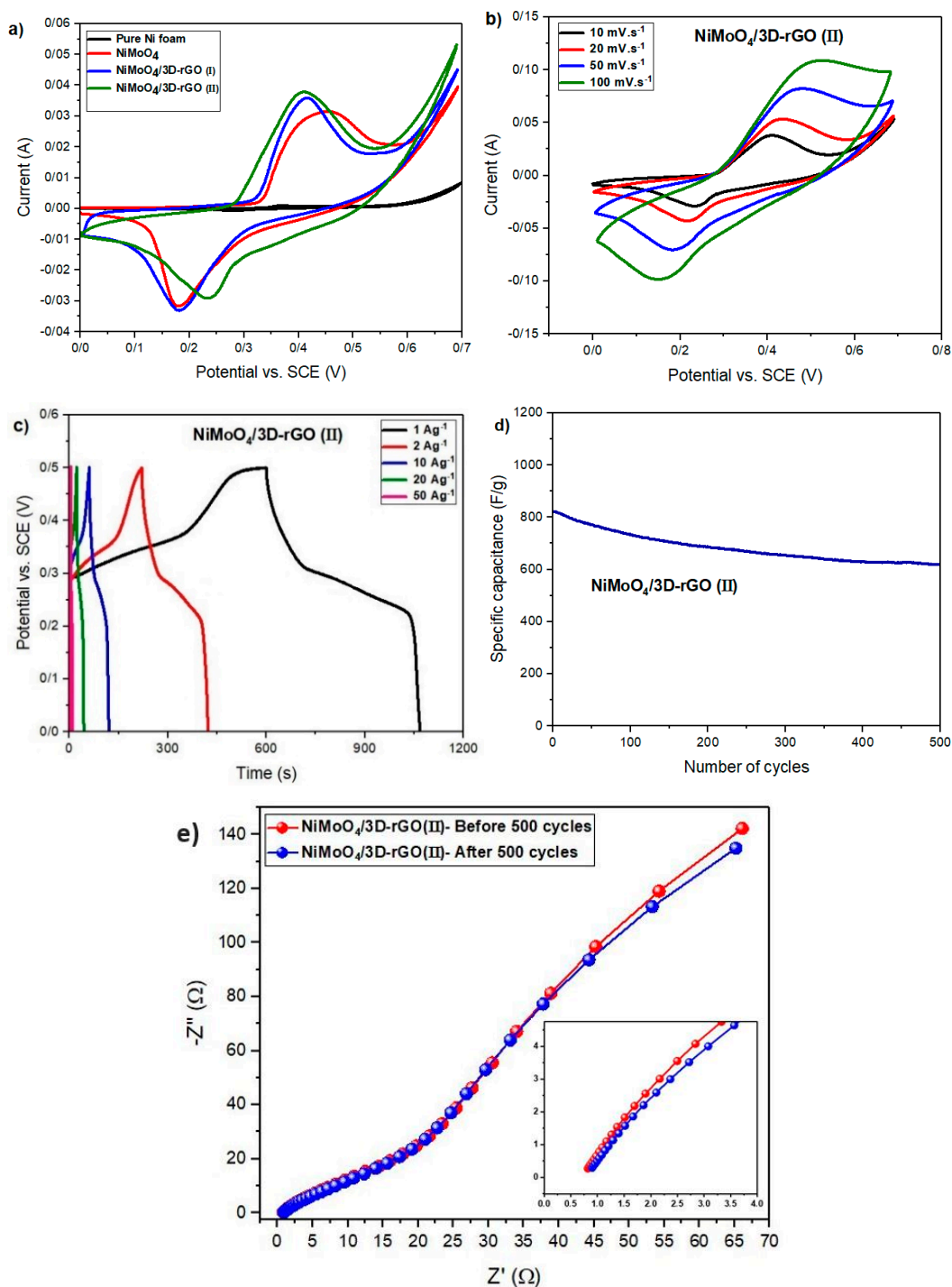


**Figure 6.** (a) Cyclic voltammetry (CV) curves of the Ni foam, NiMoO<sub>4</sub> NPs, NiMoO<sub>4</sub>/3D-rGO(I), and NiMoO<sub>4</sub>/3D-rGO(II) nanocomposites at scan rates of 10 mVs<sup>-1</sup>; (b) CV curves of the NiMoO<sub>4</sub>/3D-rGO(II) nanocomposite at different scan rates of 10–100 mVs<sup>-1</sup>; (c) GCD curves of the NiMoO<sub>4</sub>/3D-rGO(II) nanocomposite at various current densities (1–50 Ag<sup>-1</sup>); and (d) cyclic stability of the NiMoO<sub>4</sub>/3D-rGO(II) electrode after 1000 cycles; and (e) The Nyquist plots of the NiMoO<sub>4</sub>/3D-rGO(II) electrode before and after 500 cycles.

Galvanostatic charge–discharge (GCD) tests were further performed to evaluate the capacitance of the electrodes at current densities of 1–50 Ag<sup>-1</sup>. Figure 6c illustrates the GCD curves of the NiMoO<sub>4</sub>/3D-rGO(II) electrode between 0 V and 0.5 V. A pair of voltage plateaus appear at ~0.29 and ~0.23 V and nonlinear behavior of the GCD curves, revealing the pseudocapacitive features of Ni<sup>2+</sup>



ions of the NiMoO<sub>4</sub>/3D-rGO(II) electrode [18]. According to the three-electrode system, the specific capacitance of the single electrode can be estimated from the cyclic voltammetry (CV) curves and discharge curves with the Equations (8) and (9), respectively [51,52].

$$C_s = \frac{1}{m\nu \Delta V} \int IdV \quad (8)$$

$$C_s = \frac{I\Delta t}{m \Delta V} \quad (9)$$

where  $\nu$  is the scan rate,  $I$  is the discharge current,  $\Delta t$  the discharge time,  $m$  is the mass of the active material loaded on the electrode surface, and  $\Delta V$  refers to the potential range [51,52].

Stability behavior of the electrode was performed over repeated charge and discharge cycling. Therefore, GCD measurement for the NiMoO<sub>4</sub>/3D-rGO(II) electrode were carried out at a current density of 2 Ag<sup>-1</sup> for approximately 500 cycles in 3 M KOH electrolyte (Figure 6d). Initially, the NiMoO<sub>4</sub>/3D-rGO(II) electrode showed a significant decrease in the capacitance up to first 200 cycles. However, after 200 cycles the capacitance decreased slowly and at the end of 500 cycles, the capacitance dropped to 76% of its initial value. Good cycle stability of the NiMoO<sub>4</sub>/3D-rGO(II) is due to the porous structure with NiMoO<sub>4</sub> rod morphology and low amount of oxygenated groups of GO after reduction in an alkaline environment.

Figure 6e illustrates the electrochemical impedance spectra of the NiMoO<sub>4</sub>/3D-rGO(II) electrode before and after 500 cycles over the frequency range of 0.1 Hz to 100 kHz by applying a 10 mV-AC voltage. The Nyquist plots are usually consisted of two segments; the small semicircle in the high frequency region and the approximately straight line in the low frequency region. The diameter of the semicircle corresponds to the charge transfer resistance ( $R_{ct}$ ) during Faradaic redox reaction. As can be seen, the Nyquist plots of both spectra show a negligible semi-circle in the high frequency region because of fast faradaic reactions, implying low  $R_{ct}$  and good charge transfer [53]. The intercept on the real axis at the beginning of the semicircle part determine the ESR ( $R_s$ ) which is combination of electrode material resistance, ionic resistance of electrolyte and contact resistance between current collector and electrode material [54]. ESR for NiMoO<sub>4</sub>/3D-rGO(II) electrode before cycling is 0.82 and after cycling the ESR value has increased to 0.9. Moreover, the linear line in low frequency region implies Warburg impedance ( $Z_W$ ) attributed to OH<sup>-</sup> ions diffusion of electrolyte. The more vertical the line, the closer to ideal capacitive behavior of the nanocomposite [53]. In the EIS plot of NiMoO<sub>4</sub>/3D-rGO(II) electrode before 500 cycles, the straight line leans more towards the vertical  $Z''$  axis, indicating a better capacitive performance and lower ion diffusion resistance of this electrode in contrast to NiMoO<sub>4</sub>/3D-rGO(II) electrode after 500 cycles.

#### 4. Conclusions

A simple precipitation approach is demonstrated to synthesize the NiMoO<sub>4</sub> NPs, NiMoO<sub>4</sub>/3D-rGO(I) and NiMoO<sub>4</sub>/3D-rGO(II) nanocomposite electrodes. The results showed that GO sheets were successfully reduced due to the disappearance of  $2\theta = 10.6^\circ$  peak in XRD patterns and increase of  $I_D/I_G$  ratio in Raman spectrum. It can be concluded that the synergistic effect of the ammonia, metal ions and temperature benefited the deoxygenation of GO sheets. In general, addition of ammonia provided the possibility of GO deoxygenating and subsequent thermal treatment will restore the C=C bond to convert GO to reduced graphene oxide. The NiMoO<sub>4</sub>/3D-rGO(I) and NiMoO<sub>4</sub>/3D-rGO(II) electrodes demonstrated specific capacitances of 790 Fg<sup>-1</sup> and 932 Fg<sup>-1</sup>, at a current density of 1 Ag<sup>-1</sup>. An improved capacitive performance of the NiMoO<sub>4</sub>/3D-rGO(II) electrode is attributed to the pseudocapacitance behavior of NiMoO<sub>4</sub> and the elimination of oxygen-containing groups which will be beneficial to the increase in the electronic conductivity of resulting rGO. In addition, the NiMoO<sub>4</sub>/3D-rGO(II) electrode showed a good cycle life with 76% retention of the initial specific capacitance after 500 cycles.

**Author Contributions:** S.A.R.; Investigation, Synthesize and Writing—original draft, R.S.M.; Supervision, F.D.; Software, N.B.; Editing and Formal analysis, M.P.; Software, and H.O.; Supervision and editing.

**Funding:** This research received no external funding.

**Acknowledgments:** The authors acknowledge Tarbiat Modares University and Mid Sweden University for providing the facilities and technical assistance for this research. We thank the honorable supervisors, Magnus Hummelgård, and all of the personnel who work in the research.

**Conflicts of Interest:** The authors declare no conflict of interest.

## References

1. Zuo, W.; Li, R.; Zhou, C.; Li, Y.; Xia, J.; Liu, J. Battery-Supercapacitor Hybrid Devices: Recent Progress and Future Prospects. *Adv. Sci.* **2017**, *4*, 1600539. [[CrossRef](#)] [[PubMed](#)]
2. Sun, F.; Gao, J.; Zhu, Y.; Pi, X.; Wang, L.; Liu, X.; Qin, Y. A high performance lithium ion capacitor achieved by the integration of a Sn-C anode and a biomass-derived microporous activated carbon cathode. *Sci. Rep.* **2017**, *7*, 40990. [[CrossRef](#)] [[PubMed](#)]
3. Yan, A.L.; Wang, X.C.; Cheng, J.P. Research Progress of NiMn Layered Double Hydroxides for Supercapacitors: A Review. *Nanomaterials* **2018**, *8*, 747. [[CrossRef](#)]
4. Chiam, S.L.; Lim, H.N.; Hafiz, S.M.; Pandikumar, A.; Huang, N.M. Electrochemical Performance of Supercapacitor with Stacked Copper Foils Coated with Graphene Nanoplatelets. *Sci. Rep.* **2018**, *8*, 3093. [[CrossRef](#)] [[PubMed](#)]
5. Huang, L.; Zhang, W.; Xiang, J.; Xu, H.; Li, G.; Huang, Y. Hierarchical core-shell NiCo<sub>2</sub>O<sub>4</sub>@NiMoO<sub>4</sub> nanowires grown on carbon cloth as integrated electrode for high-performance supercapacitors. *Sci. Rep.* **2016**, *6*, 31465. [[CrossRef](#)] [[PubMed](#)]
6. Wang, C.; Zhou, E.; He, W.; Deng, X.; Huang, J.; Ding, M.; Wei, X.; Liu, X.; Xu, X. NiCo<sub>2</sub>O<sub>4</sub>-Based Supercapacitor Nanomaterials. *Nanomaterials* **2017**, *7*, 41. [[CrossRef](#)] [[PubMed](#)]
7. Owusu, K.A.; Qu, L.; Li, J.; Wang, Z.; Zhao, K.; Yang, C.; Zhou, L. Low-crystalline iron oxide hydroxide nanoparticle anode for high-performance supercapacitors. *Nat. Commun.* **2017**, *8*, 14264. [[CrossRef](#)] [[PubMed](#)]
8. Xue, W.D.; Wang, W.J.; Fu, Y.F.; He, D.X.; Zeng, F.Y.; Zhao, R. Rational synthesis of honeycomb-like NiCo<sub>2</sub>O<sub>4</sub>@NiMoO<sub>4</sub> core/shell nanofilm arrays on Ni foam for high-performance supercapacitors. *Mater. Lett.* **2017**, *186*, 34–37. [[CrossRef](#)]
9. Xiong, X.; Ding, D.; Chen, D.; Waller, G.; Bu, Y.; Wang, Z.; Liu, M. Three-dimensional ultrathin Ni(OH)<sub>2</sub> nanosheets grown on nickel foam for high-performance supercapacitors. *Nano Energy* **2015**, *11*, 154–161. [[CrossRef](#)]
10. Jothi, P.R.; Kannan, S.; Velayutham, G. Enhanced methanol electro-oxidation over in-situ carbon and graphene supported one dimensional NiMoO<sub>4</sub> nanorod. *Power Sources* **2015**, *277*, 350–359. [[CrossRef](#)]
11. Guo, D.; Zhang, P.; Zhang, H.; Yu, X.; Zhu, J.; Li, Q.; Wang, T. NiMoO<sub>4</sub> nanowires supported on Ni foam as novel advanced electrodes for supercapacitors. *J. Mater. Chem. A* **2013**, *1*, 9024–9027. [[CrossRef](#)]
12. Guo, D.; Luo, Y.; Yu, X.; Li, Q.; Wang, T. High performance NiMoO<sub>4</sub> nanowires supported on carbon cloth as advanced electrodes for symmetric supercapacitors. *Nano Energy* **2014**, *8*, 174–182. [[CrossRef](#)]
13. Liu, X.; Zhang, K.; Yang, B.; Song, W.; Liu, Q.; Jia, F.; Qin, S.; Chen, W.; Li, J.; Zhang, Z. Three-Dimensional Graphene Supported Nickel Molybdate Nanowires as Novel Ultralight and Flexible Electrode for Supercapacitors. *Mater. Lett.* **2016**, *164*, 401–404. [[CrossRef](#)]
14. Cai, D.; Wang, D.; Liu, B.; Wang, Y.; Liu, Y.; Wang, L.; Li, H.; Huang, Ch.; Li, Q.; Wang, T. Comparison of the Electrochemical Performance of NiMoO<sub>4</sub> Nanorods and Hierarchical Nanospheres for Supercapacitor Applications. *ACS Appl. Mater. Interfaces* **2013**, *5*, 12905–12910. [[CrossRef](#)] [[PubMed](#)]
15. Cai, D.; Liu, B.; Wang, D.; Liu, Y.; Wang, L.; Li, H.; Wang, Y.; Wang, C.; Li, Q.; Wang, T. Enhanced performance of supercapacitors with ultrathin mesoporous NiMoO<sub>4</sub> nanosheets. *Electrochim. Acta* **2014**, *125*, 294–301. [[CrossRef](#)]
16. Wu, F.; Liao, Q.; Cao, F.; Li, L.; Zhang, Y. Non-noble bimetallic NiMoO<sub>4</sub> nanosheets integrated Si photoanodes for highly efficient and stable solar water splitting. *Nano Energy* **2017**, *34*, 8–14. [[CrossRef](#)]
17. Xiao, K.; Xia, L.; Liu, G.; Wang, S.; Ding, L.X.; Wang, H. Honeycomb-like NiMoO<sub>4</sub> Ultrathin Nanosheet Arrays for High-performance Electrochemical Energy Storage. *J. Mater. Chem. A* **2015**, *3*, 6128–6135. [[CrossRef](#)]

18. Jinlong, L.; Miura, H.; Meng, Y. A novel mesoporous NiMoO<sub>4</sub>@rGO nanostructure for supercapacitor applications. *Mater. Lett.* **2017**, *194*, 94–97. [[CrossRef](#)]
19. Zhang, P.; Zhou, J.; Chen, W.; Zhao, Y.; Mu, X.; Zhang, Z.; Pan, X.; Xie, E. Constructing highly-efficient electron transport channels in the 3D electrode materials for high-rate supercapacitors: The case of NiCo<sub>2</sub>O<sub>4</sub>@NiMoO<sub>4</sub> hierarchical nanostructures. *Chem. Eng. Sci.* **2017**, *307*, 687–695. [[CrossRef](#)]
20. Huang, L.; Xiang, J.; Zhang, W.; Chen, C.; Xu, H.; Huang, Y. 3D interconnected porous NiMoO<sub>4</sub> nanoplate arrays on Ni foam as high-performance binder-free electrode for supercapacitors. *J. Mater. Chem. A* **2015**, *3*, 22081–22087. [[CrossRef](#)]
21. Nti, F.; Anang, D.A.; Han, J.I. Facilely synthesized NiMoO<sub>4</sub>/CoMoO<sub>4</sub> nanorods as electrode material for high performance supercapacitor. *Alloy Compd.* **2018**, *742*, 342–350. [[CrossRef](#)]
22. Lin, L.; Liu, T.; Liu, J.; Sun, R.; Hao, J.; Ji, K.; Wang, Z. Facile synthesis of groove-like NiMoO<sub>4</sub> hollow nanorods for high-performance supercapacitors. *Appl. Surf. Sci.* **2016**, *360*, 234–239. [[CrossRef](#)]
23. Li, Y.; Jian, J.; Fan, Y.; Wang, H.; Yu, L.; Cheng, G.; Sun, M. Facile one-pot synthesis of NiMoO<sub>4</sub>/reduced graphene oxide composite as pseudocapacitors with superior performance. *RSC Adv.* **2016**, *6*, 69627–69633. [[CrossRef](#)]
24. Bakhshali-Dehkordy, R.; Aghajani, Z. Hydrothermal-Assisted Synthesis of TiO<sub>2</sub>@NiMoO<sub>4</sub> Nanocomposites and Evaluation of Their Photocatalysis Properties. *J. Electron. Mater.* **2018**, *48*, 278–285. [[CrossRef](#)]
25. Kannan, V.; Kim, H.J.; Park, H.C.; Kim, H.S. Single-Step Direct Hydrothermal Growth of NiMoO<sub>4</sub> Nanostructured Thin Film on Stainless Steel for Supercapacitor Electrodes. *Nanomaterials* **2018**, *8*, 563. [[CrossRef](#)] [[PubMed](#)]
26. Kianpour, G.; Salavati-Niasari, M.; Emadi, H. Sonochemical synthesis and characterization of NiMoO<sub>4</sub> nanorods. *Ultrason. Sonochem.* **2013**, *20*, 418–424. [[CrossRef](#)] [[PubMed](#)]
27. Liu, T.; Chai, H.; Jia, D.; Su, Y.; Wang, T.; Zhou, W. Rapid microwave-assisted synthesis of mesoporous NiMoO<sub>4</sub> nanorod/reduced graphene oxide composites for high-performance supercapacitors. *Electrochim. Acta* **2015**, *180*, 998–1006. [[CrossRef](#)]
28. Umapathy, V.; Neeraja, P.; Manikandan, A.; Ramu, P. Synthesis of NiMoO<sub>4</sub> nanoparticles by sol–gel method and their structural, morphological, optical, magnetic and photocatalytic properties. *Trans. Nonferr. Met. Soc. China* **2017**, *27*, 1785–1793. [[CrossRef](#)]
29. Liu, M.C.; Kong, L.B.; Lu, C.; Ma, X.J.; Li, X.M.; Luo, Y.C.; Kang, L. Design and synthesis of CoMoO<sub>4</sub>-NiMoO<sub>4</sub>·xH<sub>2</sub>O bundles with improved electrochemical properties for supercapacitors. *J. Mater. Chem. A* **2013**, *1*, 1380–1387. [[CrossRef](#)]
30. Kianpour, G.; Soofivand, F.; Badieli, M.; Salavati-Niasari, M.; Hamadian, M. Facile synthesis and characterization of nickel molybdate nanorods as an effective photocatalyst by co-precipitation method. *J. Mater. Sci. Mater. Electron.* **2016**, *27*, 10244–10252. [[CrossRef](#)]
31. Chua, C.K.; Pumera, M. The reduction of graphene oxide with hydrazine: Elucidating its reductive capability based on a reaction-model approach. *Chem. Commun.* **2016**, *52*, 72–75. [[CrossRef](#)] [[PubMed](#)]
32. Yang, Z.Z.; Zheng, Q.B.; Qiu, H.X.; Jing, L.I.; Yang, J.H. A simple method for the reduction of graphene oxide by sodium borohydride with CaCl<sub>2</sub> as a catalyst. *New Carbon Mater.* **2015**, *30*, 41–47. [[CrossRef](#)]
33. De Silva, K.K.H.; Huang, H.H.; Yoshimura, M. Progress of reduction of graphene oxide by ascorbic acid. *Appl. Surf. Sci.* **2018**, *447*, 338–346. [[CrossRef](#)]
34. Zhuo, Q.; Zhang, Y.; Du, Q.; Yan, C. Facile reduction of graphene oxide at room temperature by ammonia borane via salting out effect. *J. Colloid Interface Sci.* **2015**, *457*, 243–247. [[CrossRef](#)] [[PubMed](#)]
35. Devi, M.M.; Sahu, S.R.; Mukherjee, P.; Sen, P.; Biswas, K. Graphene: A self-reducing template for synthesis of graphene–nanoparticles hybrids. *RSC Adv.* **2015**, *5*, 62284–62289. [[CrossRef](#)]
36. Bankar, P.K.; Ratha, S.; More, M.A.; Late, D.J.; Rout, C.S. Enhanced field emission performance of NiMoO<sub>4</sub> nanosheets by tuning the phase. *Appl. Surf. Sci.* **2017**, *418*, 270–274. [[CrossRef](#)]
37. Feng, H.; Cheng, R.; Zhao, X.; Duan, X.; Li, J. A low-temperature method to produce highly reduced graphene oxide. *Nat. Commun.* **2013**, *4*, 1539. [[CrossRef](#)] [[PubMed](#)]
38. Du, M.; Sun, J.; Chang, J.; Yang, F.; Shi, L.; Gao, L. Synthesis of nitrogen-doped reduced graphene oxide directly from nitrogen-doped graphene oxide as a high-performance lithium ion battery anode. *RSC Adv.* **2014**, *4*, 42412–42417. [[CrossRef](#)]
39. Soni, M.; Kumar, P.; Kumar, R.; Sharma, S.K.; Soni, A. Photo-catalytic reduction of oxygenated graphene dispersions for supercapacitor applications. *J. Phys. D Appl. Phys.* **2017**, *50*, 124003–124011. [[CrossRef](#)]

40. Ezeigwe, E.R.; Khiew, P.S.; Siong, C.W.; Tan, M.T. Synthesis of NiMoO<sub>4</sub> nanorods on graphene and superior electrochemical performance of the resulting ternary based composites. *Ceram Int.* **2017**, *43*, 13772–13780. [[CrossRef](#)]
41. Ghosh, D.; Giri, S.; Das, C.K. Synthesis, characterization and electrochemical performance of graphene decorated with 1D NiMoO<sub>4</sub>.nH<sub>2</sub>O nanorods. *Nanoscale* **2013**, *5*, 10428–10437. [[CrossRef](#)]
42. Liu, H.; Zhang, G.; Zhou, Y.; Gao, M.; Yang, F. One-step potentiodynamic synthesis of poly (1,5-diaminoanthraquinone)/reduced graphene oxide nanohybrid with improved electrocatalytic activity. *Mater. Chem. A* **2013**, *1*, 13902–13913. [[CrossRef](#)]
43. Peng, W.; Li, H.; Liu, Y.; Song, S. A review on heavy metal ions adsorption from water by graphene oxide and its composites. *Mol. Liq.* **2017**, *230*, 496–504. [[CrossRef](#)]
44. Li, Y.; Jian, J.; Xiao, L.; Wang, H.; Yu, L.; Cheng, G.; Sun, M. Synthesis of NiMoO<sub>4</sub> nanosheets on graphene sheets as advanced supercapacitor electrode materials. *Mater. Lett.* **2016**, *184*, 21–24. [[CrossRef](#)]
45. Rajkumar, M.; Hsu, C.T.; Wu, T.H.; Chen, M.G.; Hu, C.C. Advanced materials for aqueous supercapacitors in the asymmetric design. *Prog. Nat. Sci. Mater.* **2015**, *25*, 527–544. [[CrossRef](#)]
46. Jiang, G.; Zhang, M.; Li, X.; Gao, H. NiMoO<sub>4</sub>@ Ni(OH)<sub>2</sub> core/shell nanorods supported on Ni foam for high-performance supercapacitors. *RSC Adv.* **2015**, *85*, 69365–69370. [[CrossRef](#)]
47. Budhiraju, V.S.; Kumar, R.; Sharma, A.; Sivakumar, S. Structurally stable hollow mesoporous graphitized carbon nanofibers embedded with NiMoO<sub>4</sub> nanoparticles for high performance asymmetric supercapacitors. *Electrochim. Acta* **2017**, *238*, 337–348. [[CrossRef](#)]
48. Yang, J.; Liu, W.; Niu, H.; Cheng, K.; Ye, K.; Zhu, K.; Yan, J. Ultrahigh energy density battery-type asymmetric supercapacitors: NiMoO<sub>4</sub> nanorod-decorated graphene and graphene/Fe<sub>2</sub>O<sub>3</sub> quantum dots. *Nano Res.* **2018**, *11*, 4744–4758. [[CrossRef](#)]
49. Wei, C.; Huang, Y.; Yan, J.; Chen, X.; Zhang, X. Synthesis of hierarchical carbon sphere@NiMoO<sub>4</sub> composite materials for supercapacitor electrodes. *Ceram Int.* **2016**, *42*, 15694–15700. [[CrossRef](#)]
50. Zhang, Z.; Liu, Y.; Huang, Z.; Ren, L.; Qi, X.; Wei, X.; Zhong, J. Facile hydrothermal synthesis of NiMoO<sub>4</sub>@CoMoO<sub>4</sub> hierarchical nanospheres for supercapacitor applications. *Phys. Chem. Chem. Phys.* **2015**, *17*, 20795–20804. [[CrossRef](#)]
51. Yang, S.; Zhang, K. Converting Corn cob to Activated Porous Carbon for Supercapacitor Application. *Nanomaterials* **2018**, *8*, 181. [[CrossRef](#)] [[PubMed](#)]
52. Krishnan, S.G.; Ab Rahim, M.H.; Jose, R. Synthesis and characterization of MnCo<sub>2</sub>O<sub>4</sub> cuboidal microcrystals as a high performance pseudocapacitor electrode. *Alloy. Compd.* **2016**, *656*, 707–713. [[CrossRef](#)]
53. Fang, L.; Wang, F.; Zhai, T.; Qiu, Y.; Lan, M.; Huang, K.; Jing, Q. Hierarchical CoMoO<sub>4</sub> nanoneedle electrodes for advanced supercapacitors and electrocatalytic oxygen evolution. *Electrochim. Acta* **2018**, *259*, 552–558. [[CrossRef](#)]
54. Miankushki, H.N.; Sedghi, A.; Baghshahi, S. Facile and scalable fabrication of graphene/polypyrrole/MnO<sub>x</sub>/Cu(OH)<sub>2</sub> composite for high-performance supercapacitors. *J. Solid State Chem.* **2018**, *22*, 3317–3329. [[CrossRef](#)]

